Physica A 450 (2016) 585–600

Contents lists available at ScienceDirect

Physica A

journal homepage: www.elsevier.com/locate/physa

Irreversibility and complex network behavior of stream flow fluctuations

Francesco Serinaldi *, Chris G. Kilsby

School of Civil Engineering and Geosciences, Newcastle University, Newcastle Upon Tyne, NE1 7RU, UK
Willis Research Network, 51 Lime St., London, EC3M 7DQ, UK

HIGHLIGHTS

- Stream flows across the United States are analyzed by directed visibility graphs.
- Directed horizontal visibility graphs highlight irreversibility and nonlinearity.
- Nonlinearity conceals linear short and long range dependence.
- Degree distributions exhibit spatially coherent subexponential behavior.
- Hydrological and physical interpretation of stream flow nonlinearity is provided.

ARTICLE INFO

Article history:
Received 23 October 2015
Received in revised form 18 December 2015
Available online 21 January 2016

Keywords:
Visibility graphs
Stream flow
Network analysis
Nonlinearity
Irreversibility
US rivers

ABSTRACT

Exploiting the duality between time series and networks, directed horizontal visibility graphs (DHVGs) are used to perform an unprecedented analysis of the dynamics of stream flow fluctuations with focus on time irreversibility and long range dependence. The analysis relies on a large quality-controlled data set consisting of 699 daily time series recorded in the continental United States (CONUS) that are not affected by human activity and primarily reflects meteorological conditions. DHVGs allow a clear visualization and quantification of time irreversibility of flow dynamics, which can be interpreted as a signature of nonlinearity, and long range dependence resulting from the interaction of atmospheric, surface and underground processes acting at multiple spatio-temporal scales. Irreversibility is explored by mapping the time series into ingoing, outgoing, and undirected graphs and comparing the corresponding degree distributions. Using surrogate data preserving up to the second order linear temporal dependence properties of the observed series, DHVGs highlight the additional complexity introduced by nonlinearity into flow fluctuation dynamics. We show that the degree distributions do not decay exponentially as expected, but tend to follow a subexponential behavior, even though sampling uncertainty does not allow a clear distinction between apparent or true power law decay. These results confirm that the complexity of stream flow dynamics goes beyond a linear representation involving for instance the combination of linear processes with short and long range dependence, and requires modeling strategies accounting for temporal asymmetry and nonlinearity.

1. Introduction

The stream flow process is a result of the interaction between meteorological and catchment processes. Therefore, the complexity of recorded runoff signals (hydrographs) and their properties reflects the complexity of such geophysical systems

* Corresponding author at: School of Civil Engineering and Geosciences, Newcastle University, Newcastle Upon Tyne, NE1 7RU, UK.
E-mail address: francesco.serinaldi@ncl.ac.uk (F. Serinaldi).

http://dx.doi.org/10.1016/j.physa.2016.01.043

and their interplay. Two important characteristics of stream flow fluctuations are irreversibility (or temporal asymmetry) and persistence (or long range dependence). A stationary process is statistically time reversible if a time series and its time reversed equivalent have the same joint distribution, i.e. they are equally probable [1]. Time irreversibility indicates the presence of nonlinearity of the underlying dynamics, such as dissipative chaos, and is related to out-of-equilibrium driven systems in thermodynamics [2,3]. In the context of river dynamics, time irreversibility, and thus nonlinearity, depends on the different processes driving the flow process in the periods of increasing discharge (the so-called hydrograph's rising limbs) and decreasing discharge (hydrograph's recession limbs). Rising limbs are driven by meteorological forcings that evolve at relatively short time scales, which are essentially the characteristic scales of rainfall dynamics (from minutes to weeks, according to the convective or advective nature of the meteorological system at play). On the other hand, recession limbs reflect the ground water dynamics, i.e. the progressive reduction of the water content stored in the ground in the early rising phase, and evolve at larger time scales (up to months). These different mechanisms make the rising limb steeper than the recession limb, whereby the first can be interpreted as a phase in which meteorological impulses drive the river system out of equilibrium, while the latter describe the slower recovery phase. Serinaldi and Kilsby [4] recently quantified irreversibility in a large data set of flow signals referring to 473 European stream gage stations by using the temporal third moment function [5].

The above dynamics are further complicated by additional factors influencing the river system at larger time scales, such as climate fluctuations acting at decade to century (or even longer) time scales. The same holds for the geomorphological evolution of the river network, land cover, and soil and underground changes. All these mechanisms introduce slowly varying fluctuations in the flow dynamics, and thus dependence between observations far in time from each other. This behavior is referred to as persistence or long range dependence, is usually quantified by the Hurst parameter H [6], and has been widely studied in the physical and hydrological literature owing to its importance in analysis, modeling, and prediction of hydro-meteorological systems [7–11]. In particular, Serinaldi and Kilsby [4] showed that some main characteristics of stream flow fluctuations can be explained by the interaction of short and long range dependence, and can be modeled by the so-called generalized Hurst–Kolmogorov (gHK) process [12], which couples a first-order autoregressive process describing short range dependence and the Hurst–Kolmogorov process (also known as fractional Gaussian noise) for long range dependence. However, gHK (along with other processes commonly applied in time series analyses) is reversible and cannot reproduce flow signal irreversibility.

In this context, combining linear and nonlinear time series analyses can allow a better characterization of complex signals [13–15]. Among the available methods, mapping procedures of time series into network graphs allow us to apply graph theoretical tools developed in complex network theory [16–19]. One of these methods, called the visibility graph (VG) algorithm [20,21] has been applied to study several geophysical systems such as hurricanes [22], seismicity [23,24], ocean tides [25], wind speed [26], and solar activity [27]. A particular version of VG, called horizontal visibility mapping algorithm [28] (hereinafter HVG), was shown to capture series properties such as periodicity, fractality, and chaoticity, thus translating them into corresponding visibility graphs [16]. The directed version of HVG, referred to as directed HVG (DHVG) [1] also allows us to highlight irreversibility, and quantifying it by information theory measures, such as Kullback–Leibler (K–L) relative entropy measure [1], and classical statistical tests, such as Kolmogorov–Smirnov goodness-of-fit test [29]. Therefore, DHVG is a suitable candidate tool to explore jointly both persistence and irreversibility in stream flow series.

In this study, we built on a recent study focused on HVG analysis and Brazilian rivers [30], and perform an unprecedented large scale study, applying DHVG to a quality controlled daily runoff data set including 699 time series that span up to 114 years, are not affected by anthropogenic interventions, and are specifically devised for climate-related studies. This makes the analysis free from possible artifacts related to anthropogenic activities, thus focusing on the actual properties of natural flow fluctuations. The paper is structured as follows. Data and methodology are presented in Section 2. Results are discussed in Section 3, while Section 4 provides conclusions.

2. Data and methods

2.1. Stream flow data set and preprocessing

The data set used in this study comprises 699 daily stream flow time series extracted from the Hydro-Climatic Data Network (HCDN-2009) [31], which is composed of 743 gage stations maintained by the US Geological Survey (USGS). This data set is a subset of the wider USGS GAGES-II (Geospatial Attributes of Gages for Evaluating Streamflow, version II) reference stations providing geospatial data and classifications for 9322 stream gages. HCDN-2009 includes quality-controlled time series from stations that were screened to exclude sites where human activities or other activities affect the natural flow, and with length sufficiently long for analysis of patterns in stream flow over time. HCDN-2009 is specifically drawn to provide a stream flow data set suitable for analyzing hydrologic variations and trends in a climatic context [31]. Fig. 1 shows the study area and stream gage locations, the time series of the number of stations available in a given year (out of 699), and the histogram of the available record length. A complete list of HCDN-2009 stations along with basic attributes can be found at the web site http://water.usgs.gov/osw/hcdn-2009/, while the data set is freely available at http://waterdata.usgs.gov/nwis/sw.

To filter out the effect of the seasonality, all time series have been preliminarily preprocessed as follows. For a given sequence of stream flow observations $\{x_t\}_{t=1,\ldots,N}$, where N is the sample size, the empirical average value for each calendar

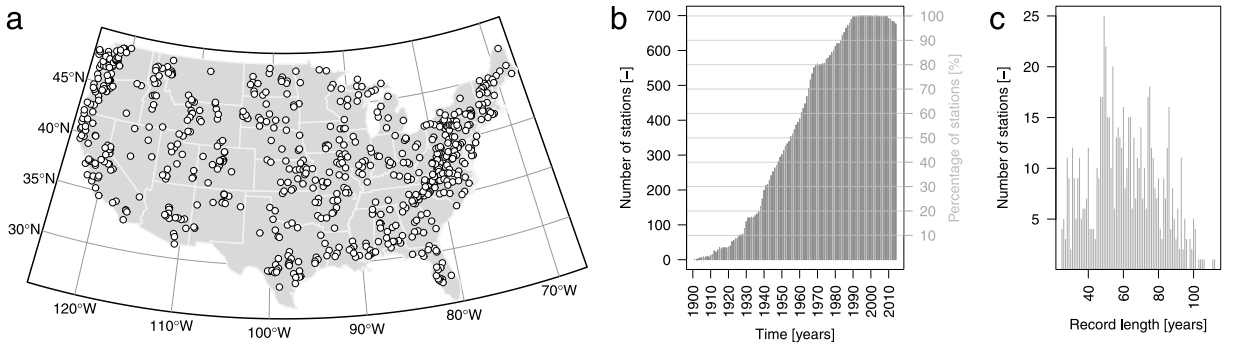

Fig. 1. Study area and stream gage locations (a), time series of the number of stations available in a given year out of 699 (b), and histogram with the available record length (c). For instance, panel (b) indicates that the data for almost all stations are available only for the period after the late 1980's, while the frequency function in panel (c) indicates that the average length of the time series is about 60 years.

day $\{\tilde{m}_i\}_{i=1,\ldots,365}$ and the calendar-day standard deviation $\{\tilde{s}_i\}_{i=1,\ldots,365}$ are computed. The seasonal components $\tilde{m}_i$ and $\tilde{s}_i$ are then smoothed by local scatter plot smoothing (LOESS) [32] following the rationale of the seasonal-trend decomposition based on LOESS (STL) procedure [33], obtaining smoothed seasonal components m_i and s_i. Thus, deseasonalized time series y_t are obtained by subtracting m_i from x_t and then dividing by s_i as follows

$$y_{i,t} = \frac{x_{i,t} - m_i}{s_i}, \quad \text{for } i = 1, \ldots, 365 \quad \text{and} \quad t = 1, \ldots, N. \tag{1}$$

This procedure removes the seasonality of the first two moments of the time series acting approximately as a band-pass filter extracting signal frequencies in the range within about one month and one year, and is standard preprocessing procedure in this kind of hydrological analyses [7–9,34].

2.2. Horizontal visibility graphs

In this study we use the horizontal visibility algorithm introduced by Luque et al. [28] as a special case of the visibility algorithm [20,21] to map stream flow time series into graphs. Referring to Luque et al. [28] for the original description, the algorithm is as follows. Given a generic time series $\{x_t\}_{t=1,\ldots,N}$, each observation corresponds to a node in the HVG. Two nodes i and j are connected if one can draw a horizontal line in the time series connecting x_i and x_j without intersecting any intermediate observation. This means that two connected nodes i and j fulfill the geometrical criterion within the time series

$$x_i, x_j > x_t, \quad \forall t \mid i < t < j. \tag{2}$$

HVG has a number of properties making it a useful diagnostic tool [28]:

(i) Connection: each node sees at least its left-side and right-side nearest neighbors.
(ii) Invariance under affine (monotonic) transformations, making it a nonparametric rank-based method which is insensible to rescaling procedures.
(iii) Data compression (reversibility between time series and network representation): Since the network structure is completely defined by the binary adjacency matrix, some information concerning the actual value of each observation is unavoidably lost; however, this limit is common to every nonparametric rank-based method, and can be overcome by using weighted networks.
(iv) Exponential degree distribution: recalling that the degree distribution of a graph describes the probability of an arbitrary node to have k links (degree k), it can be shown that random, chaotic, and stochastic processes (with exponentially and power law decaying autocorrelation) map into graphs with exponential probability density function (PDF) of degrees, $p(k) \propto \exp(-\lambda k)$, where the value of λ characterizes the specific process [16].
(v) Directed and indirected characters of the mapping: the algorithm allows the definition of undirected graphs mapping the links between each observation x_t with *past* and *future* observations, or directed graphs, whereby we can distinguish two degrees for each given node: an ingoing degree $k_{\text{in}}(t)$, which is the number of links of node t with other past nodes corresponding with data in the series (i.e., nodes with $t' < t$), and an outgoing degree $k_{\text{out}}(t)$, which is the number of links with future nodes ($t' > t$). The ingoing and outgoing degree distributions of a DHVG are defined as the PDFs of k_{in} and k_{out} of the graph [28,1], referred to as $p_{\text{in}}(k) := \mathbb{P}[k_{\text{in}} = k]$ and $p_{\text{out}}(k) := \mathbb{P}[k_{\text{out}} = k]$.

When the DHVG is not invariant under time reversion (i.e. the degree distribution $p_{\text{in}}(k)$ is different from $p_{\text{out}}(k)$), therefore one can state that the generating process is not conservative. As mentioned above, time irreversibility is an expected characteristic of stream flow dynamics due to the different physical processes involved in the hydrograph rising

and recession limbs, which describe departure from equilibrium (related to meteorological impulses) and subsequent recovery.

To better understand the properties of stream flow fluctuations, the directed degree distributions of the observed series have been compared with those of two types of surrogate data: (i) time independent shuffled data preserving the marginal distribution, and (ii) iterative amplitude adjusted Fourier transformation (IAAFT) [35,36,5,37,38] preserving almost exactly the marginal distribution function and power spectrum of the observations, i.e. the linear moments up to the second order. IAAFT surrogates are stationary [39] and temporally symmetric by construction because of randomization of Fourier phases, meaning that the sampling algorithm does not preserve the possible forward–backward asymmetry of the original signal. Therefore, IAAFT is often used in nonlinear dynamics studies to check nonlinear behavior.

2.3. Inference procedure on degree distributions

Since the empirical results reported in Section 3 show that the empirical degree distributions of flow data depart from the theoretical exponential behavior characterizing processes with linear temporal dependence, we set up a detailed frequency analysis to better understand the nature of such distributions. The analysis involves five candidate distributions describing different tail behavior, going from hyperexponential (upper tail lighter that exponential) to subexponential (tail heavier than exponential) [40–42]. In more detail, we consider the exponential distribution (EXP) as a benchmark, Pearson type III (PE3; also known as shifted gamma), Generalized Pareto (GP), Weibull (WEI; also known as stretched exponential), and lognormal (LN3). Referring to the literature for further details and to the Appendix for the parameterization of these models, we recall some key properties.

In this set of distributions, GP is the only power-type model exhibiting asymptotic behavior similar to $x^{-1/\xi}$ for $\xi > 0$ (where x denotes a generic random variable, and ξ is the GP shape parameter in Eq. (A.3)), while the others are of exponential kind. For $\xi = 0$, GP degenerates to the exponential distribution, thus making GP a suitable model to investigate possible power law decay related for instance to scale-free networks. The PE3 distribution in Eq. (A.2) has a "slightly lighter" tail than the exponential as it decays faster, while, for $\xi > 1$, PE3 exhibits a "slightly heavier" tail decaying more slowly than exponentially [42, and references therein]. The WEI distribution (Eq. (A.4)) can have either an apparent heavy or bounded tail depending on the value of its shape parameter in a penultimate sense [43–45]. The LN3 distribution (Eq. (A.5)) is also considered a heavy-tailed distribution (it belongs to the subexponential family) and can approximate power law distributions for a large portion of the body of the distribution [46,42].

Exploratory data analysis is performed by using the L-moment ratio diagrams (LMRDs), which are similar to the conventional moment ratio diagrams [47], but relying of the L-moments (where "L" stands for linear combination of order statistics). L-moment framework [48,49] is widely used in the hydrological frequency analysis as it shows several advantages compared to conventional moments. For instance, L-moments are less sensitive to outliers and are more reliable, thus increasing the diagnostic power of ratio diagrams. L-moments of every order do exist provided the existence of the first one, which corresponds to the mean. L-moment framework also provides an estimation method performing similarly to or better than maximum likelihood in terms of bias and variance for small sample sizes.

Based on the above remarks and model selection purposes discussed later, distributions' parameters are estimated by three different methods: (i) L-moments (LM), (ii) maximum likelihood (ML), and (iii) the minimization of the following modified mean square error (MSE) norm defined as [42]

$$\mathrm{MSE} = \frac{1}{N}\sum_{i=1}^{N}\left(\frac{S(x_{i:N})}{S_N(x_{i:N})} - 1\right)^2, \tag{3}$$

where $S = 1-F$ denotes the survival function corresponding to a parametric cumulative distribution function F, $S_N = 1-F_N$ is the empirical counterpart where F_N is estimated by the Weibull plotting position formula $F_N(x) = 1/(N+1)\sum \mathbf{1}_{\{x_i \le x\}}$, and $x_{i:N}$ is the ith order statistic. This norm was shown to be unbiased, exhibiting also lower variance in comparison to other candidates, such as the conventional MSE computed on the quantiles [42]. MSE considers the relative error between the theoretical and the empirical values of the cumulative distribution functions rather than using the x values [42]. To assess the effect of the sample size, we defined the degree distributions of HVG for annual subsamples and the entire time series (hereinafter referred to as annual series and global series, respectively). All distributions are therefore fitted over the range $k > 2$ for annual series, and $k > 4$ for global series to reduce the effect of departures from the theoretical laws due to discretization effect for small degrees, but retaining enough data for algorithms' convergence.

After model parameter estimation, goodness of fit was assessed by using MSE, as this norm is formally close to other well-known goodness-of-fit measures based on cumulative distribution functions such as Kolmogorov–Smirnov or Cramer–von Mises [50], thus making it a suitable norm to assess model fitting. Of course, when parameters are estimated by minimizing MSE, the resulting MSE values are expected to be smaller than MSE values computed for the models resulting from LM and ML estimation methods, because in these cases optimal parameters correspond to criteria different from MSE. Thus, MSE should be used to compare the performance of the five candidates for each estimation method separately.

Finally, model selection is performed applying two criteria. First, for all three estimation methods, the "best" fitted model or "optimal" model is considered to be the one with the smallest MSE. However, MSE does not give information about the degree of likelihood of each model, and thus the significance of the difference among different candidates. Therefore, as

a second criterion, we exploit ML method to implement a model selection based on information theory criteria [51]. In particular, we use the bias corrected Akaike information criterion (AIC) [52]

$$\mathrm{AIC_c} := -2\log(\mathcal{L}(\hat{\theta})) + 2M + \frac{2M(M+1)}{N-M-1} \equiv \mathrm{AIC} + \frac{2M(M+1)}{N-M-1}, \tag{4}$$

where M is the number of parameters and N is the sample size. $\mathrm{AIC_c}$ values are used to compute the differences [51, pp. 70–72]

$$\Delta_j := \mathrm{AIC}_{c,j} - \mathrm{AIC}_{c,\min}. \tag{5}$$

Such differences quantify the relative expected K–L differences between the unknown true distribution G and the fitted models $F_i(x|\theta)$, where θ denotes a generic vector of parameters estimated by ML. These Δ_j values are easy to interpret and allow a quick comparison and ranking of candidate models. The model estimated to be optimal has $\Delta_j \equiv \Delta_{\min} \equiv 0$ [51, pp. 70–72]. The quantities $\exp(\Delta_j/2)$ correspond to the evidence ratios, when we compare the evidence for the best model versus the jth optimal model. They represent the evidence about fitted models as to which is better in the K–L information sense [51, pp. 77–79]. For instance, for $\Delta_j = 2$, the evidence ratio is 2.7, meaning that the estimated best model is 2.7 times as probable as the jth model to minimize the information loss, or vice versa the jth model is $1/2.7 = 0.368$ times as probable as the estimated best model to minimize the information loss. A rule of thumb for model selection is as follows [51, p. 70]: $\Delta_j \in (0, 2)$ gives a substantial support for model j, $\Delta_j \in (4, 7)$ considerably less, $\Delta_j > 10$ essentially none. We use Δ_j values to select the best model (analogously to MSE selection) and to check the number of models falling in the interval $(0, 2)$; this gives an overall picture about the strength of evidence for the best fitted model. Indeed, if several models show Δ_j values in the range $(0, 2)$, this means that these models are all plausible candidates in the K–L information sense, under the hypothesis that one of the models must be the K–L best model of that set of models.

In summary, the inference includes five different distributions (EXP, PE3, GP, WEI, and LN3), three estimation methods (LM, MSE, and ML), and two goodness-of-fit/model selection criteria (MSE and $\mathrm{AIC_c}$).

3. Results and discussion

3.1. Analysis of degree distributions

For the sake of comparison with previous findings reported in the literature [30], a first visual check is performed by using survival functions $S(k) = 1-F(k) = \mathbb{P}[K > k]$. Fig. 2 shows the diagrams of $S(k)$ versus k corresponding to ingoing, outgoing and undirected HVGs for the observed, shuffled and IAAFT series. Focusing on the undirected graphs, based on results concerning Brazilian stream flow series [30], we expected an exponential decay of the upper tail of degree distributions faster than random, corresponding to stochastic processes with temporal dependence [16]; however, the diagrams show that the degree distributions decay more slowly than exponentially on a double logarithmic plot, thus indicating a possible algebraic heavy tail behavior. This subexponential decay is even more evident by comparing the degree distributions of the observed series with those of shuffled and IAAFT signals. For shuffled data, $S(k)$ functions decay exponentially as expected and are coherent with the theoretical exponential distributions describing a random process ($\lambda = \ln(3/2)$ and $\lambda_{\mathrm{in}} = \lambda_{\mathrm{out}} = \ln(2)$). Since IAAFT sequences preserve the autocorrelation (power spectrum) of the original series, we expect a decay faster than the theoretical one for random signals. However, as the annual subsampling can conceal this behavior owing to the limited sample size, we also considered HVGs for the global series. Fig. 3 shows the corresponding $S(k)$ functions, which confirm the subexponential behavior for the observed series, the exponential decay for shuffled signals, and the faster-than-random exponential decay of the IAAFT sequences.

To better understand the actual nature of the observed degree distributions, $S(k)$ diagrams are complemented by LMRDs of L-kurtosis τ_4 versus L-skewness τ_3 (Fig. 4). Each panel of Fig. 4 shows the empirical pairs (τ_3, τ_4) superimposed to the theoretical curves corresponding to PE3, GP, WEI and LN3 models, and the theoretical point describing the EXP distribution for whatever parameters' values. Each panel displays observed, shuffled, and IAAFT samples and the median values of each cloud of points. Focusing on the annual scale in the top panels of Fig. 4, the discrepancy between the observed and shuffled and IAAFT L-moments is remarkable. In particular, the observed L-moments cover a wider range of values on the right side of the point denoting the EXP distribution, corresponding to distributions more skewed than EXP. The median points of the observed L-moments are close to GP theoretical line for ingoing degree distributions, to LN3 for outgoing, and lie between GP and LN3 for undirected, thus confirming the difference between ingoing and outgoing behavior already recognized in the $S(k)$ diagrams, and the mixing effect characterizing the undirected distributions. On the other hand, shuffled and IAAFT L-moments overlap to each other almost perfectly, cover smaller ranges of values, and are centered around the theoretical EXP point as expected. Moreover, ingoing and outgoing samples of shuffled and IAAFT L-moments are very similar, while for undirected samples, IAAFT L-moments tend to move slightly on the left side of the theoretical EXP point, confirming the hyperexponential behavior of the undirected degree distributions of signals with linear long range dependence. Bottom panels of Fig. 4 further support the above analysis relying on longer global series, which remarkably reduce the uncertainty (variability) of the sample L-moments. However, while conclusions are kept unchanged for shuffled and IAAFT data, the median of observed ingoing L-moments is between GP and WEI curves, the median of observed outgoing L-moments is between GP and LN3 curves, and the median of observed undirected L-moments is close to GP curve. In all cases, the

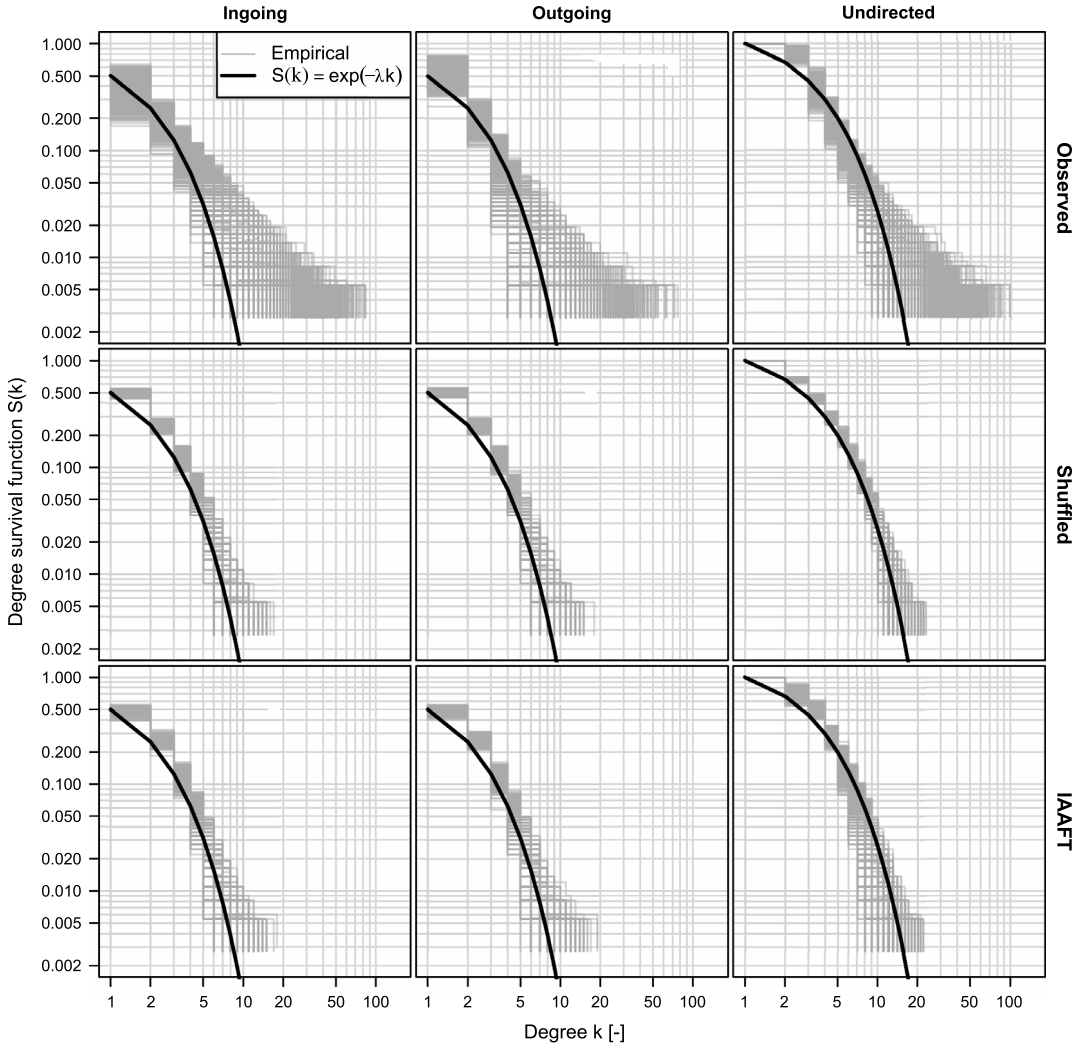

Fig. 2. Survival functions $S(k)$ of HVGs degrees for annual subseries on a double logarithmic scale. Rows of panels show results for observed, shuffled, and IAAFT data, while columns report density functions for ingoing, outgoing, and undirected networks. Black lines denote the expected theoretical exponential $S(k) \propto \exp(-\lambda k)$ for temporally independent random noise. The discrepancies between the observed $S(k)$ functions and the exponential model (top panels) disappear for shuffled and IAAFT data (middle and bottom rows of panels). Since IAAFT preserves up to second order linear moments, the behavior of the observed $S(k)$ functions can be attributed to nonlinear dynamics.

range of empirical L-moments denotes the presence of degree distributions whose behavior goes from EXP or slightly hyperexponential to evident subexponential.

In order to quantitatively assess which theoretical model better describes the empirical degree distributions, the five models are fitted to data by LM, MSE, and ML methods, then assessing the fitting accuracy in terms of MSE. Results for annual series are reported in Fig. 5, where each panel shows the box plots of MSE for the five models fitted by the three estimation methods. As mentioned in Section 2.3, the smallest MSE values are obtained when MSE itself is minimized to estimate the parameters; so, the relative goodness of fit of the five distributions should be assessed for each estimation method separately. For example, focusing on the ingoing observed degree distributions, GP, WEI, and LN3 show similar MSE for the LM method; using MSE minimization, GP and LN3 yield smaller MSE values, while GP seems to be the best model when parameters are fitted by ML. Extending the analysis to outgoing and undirected cases, GP and LN3 always provide the better fit in terms of MSE, while EXP always provides poor results. Unlike what is expected, for shuffled and IAAFT data, EXP exhibits again the largest MSE along with LN3, while PE3, GP, and WEI generally yield similar MSE. This is only apparently surprising because sampling fluctuations introduce discrepancies from the expected two-parameter EXP behavior that are better captured by the three-parameter competitors including EXP as a special case. Notice that LN3 is a credible alternative in terms of MSE only when this norm is used to fit the parameters.

As for the LMRDs, results are slightly different moving from annual to global scale (Fig. 6). In particular, focusing on the observed data, GP is no longer the best option for ingoing and undirected cases, but it is outperformed by WEI when the

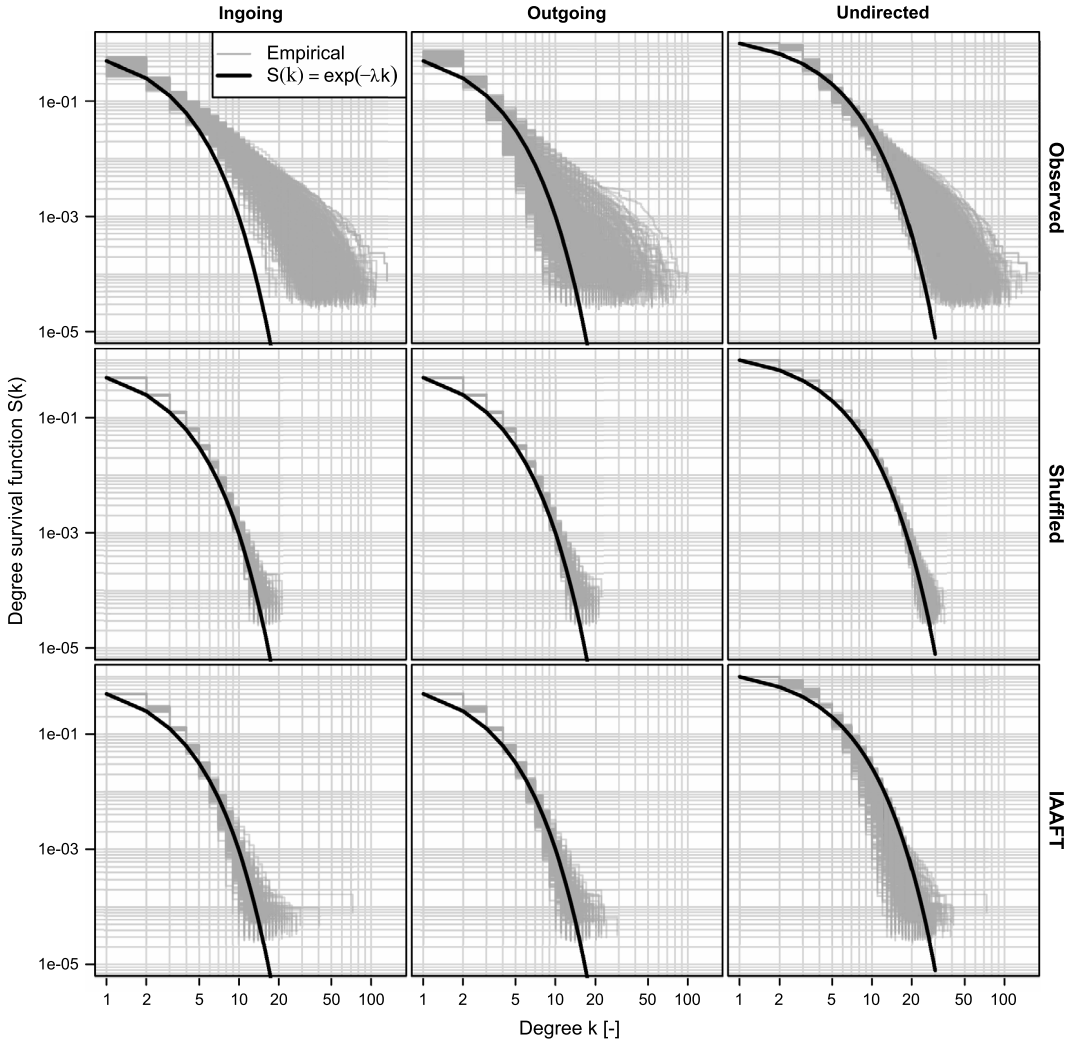

Fig. 3. As for Fig. 2, but for networks defined on the global series (without splitting in annual subsets); similar interpretation applies.

model is fitted by LM. On the other hand, GP and LN3 perform very close to each other for outgoing distributions. Above remarks on annual data still apply for global shuffled and IAAFT cases, with GP being generally the optimal model, and LN3 the worst.

The previous MSE analysis gives an overall picture of the fitting performance, but it does not give information about which model should be selected in each case. This task is accomplished by identifying which model shows the smallest MSE and AIC_c for each empirical degree distribution. MSE can be applied for all estimation methods but it does not account for the different number of parameters of EXP and the other models, and does not allow the assessment of the significance of MSE differences between the best model and the others. On the other hand, AIC_c accounts for the latter two aspects but can be coherently applied only for ML estimates. Results are summarized in terms of percentage of times each model is selected as the optimal one.

For annual scale and observed data (Fig. 7), GP and LN3 are the dominant models when MSE is used as selection criterion independently of the fitting method, with GP being the most frequent option for ingoing case, and LN3 for outgoing and undirected. However, using AIC_c, WEI and GP are the best options for ingoing distributions, while GP dominates for outgoing and undirected distributions. Looking at shuffled and IAAFT results, GP is generally the most frequent optimal model, except when the model is fitted and selected by MSE; in this case, GP and LN3 have similar selection rate. Results become clearer for global data (Fig. 8). GP and WEI are the best models for observed outgoing and undirected distributions, while LN3 and partly GP dominate for outgoing case and MSE selection, but in this case GP is the definite winner using AIC_c. Looking at global shuffled and IAAFT data, LN3 is generally outperformed by the other models including EXP as a special case, and GP is the definite winner for AIC_c selection. Finally, $\Delta_j < 2$ in the $\approx$ 25% and $\approx$ 1% of cases for annual data and global data, respectively. This means that in the $\approx$ 25% of cases for annual data, two or more models are possible candidates minimizing

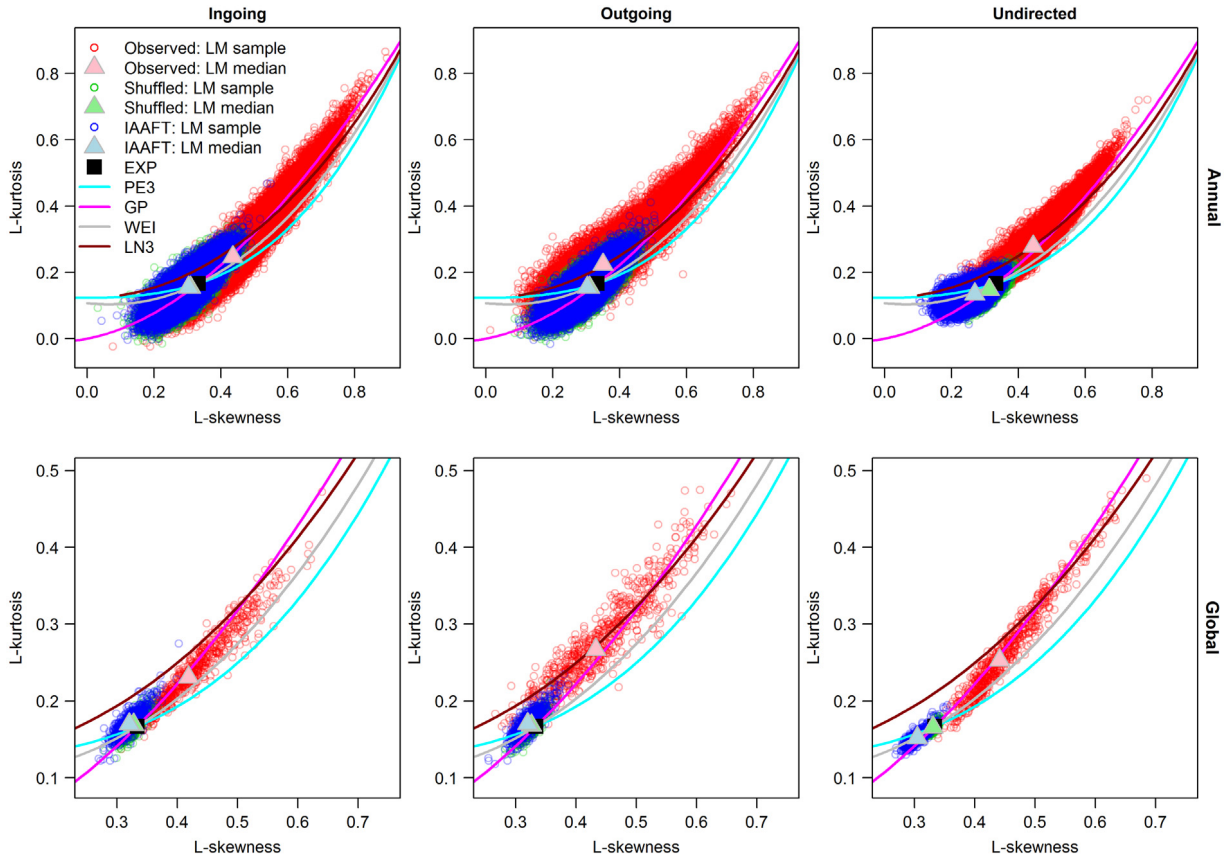

Fig. 4. LMRDs for ingoing (left side), outgoing (middle), and undirected (right side) degree distributions for annual (top) and global data (bottom). For each panel, empirical pairs of L-kurtosis τ_4 and L-skewness τ_3 are superimposed to the theoretical curves corresponding to PE3, GP, WEI, and LN3 models, and the theoretical point describing the EXP distribution. The median value of each cloud of points is also shown. LMRDs indicate that: (i) shuffled degree distributions are close to EXP point as expected, (ii) IAAFT degree distributions tend to be exponential (for ingoing and outgoing cases) or hyperexponential (for undirected case), and (iii) observed degree distributions tend to follow GP/WEI (ingoing), GP/LN3 (outgoing), and GP (undirected).

the K–L information loss, thus confirming the uncertainty of conclusions relying on annual degree distributions. On the other hand, stronger evidence supports the selected optimal model when using global data.

To summarize, LMRDs, MSE analysis, and model selection provide a coherent picture indicating that:

1. For annual data, ingoing distributions are close to GP and WEI with more support for the first, outgoing distributions are close to GP or LN3, and undirected distributions are close to GP or WEI/LN3. Owing to sampling uncertainty, a definite choice is not possible because model selection yields two or more optimal models (in the K–L loss sense) in the $\approx 25\%$ of cases. This suggests that the information (in the theoretic information sense) contained in annual subsets of daily data might be not sufficient to draw reliable conclusions even on the nature of the body of degree distributions.
2. For the global data, model selection yields a single optimal models (in the K–L loss sense) in the $\approx 99\%$ of cases. However, similar to annual data, selection does not indicate a unique distribution. Indeed, GP, WEI, and LN3 alternate as possible optimal choices with prevalence of GP.
3. Bearing in mind that GP, WEI, and LN3 have heavy tail subexponential behavior, but GP is the only one exhibiting a real asymptotic power law tail, our findings confirm the difficulty to draw definite conclusions about the actual asymptotic nature of the degree distributions from finite samples. This difficulty is well known in the literature [46], and is related not only to the similar asymptotic or pre-asymptotic behavior of GP, WEI, and LN3 but also to common generating processes. In fact, power law and lognormal decay can result from slightly different multiplicative processes with and without a bounded minimum acting as a lower reflective barrier to the multiplicative model [46], while power law and stretched exponential correspond to linear and sublinear preferential attachment mechanisms, respectively [53]. Therefore, the combined effect of distribution similarities, possible common generating mechanisms, and finite sample sizes can likely explain the ambiguity of model selection outcomes.
4. EXP distribution is rarely selected as the best model even for the cases (shuffled and IAAFT) in which it is the expected theoretical model. However, as discussed above, sampling fluctuations generate discrepancies (see the scattering of L-moments in Fig. 4) that are better described by distributions with an additional parameter, including EXP as a special

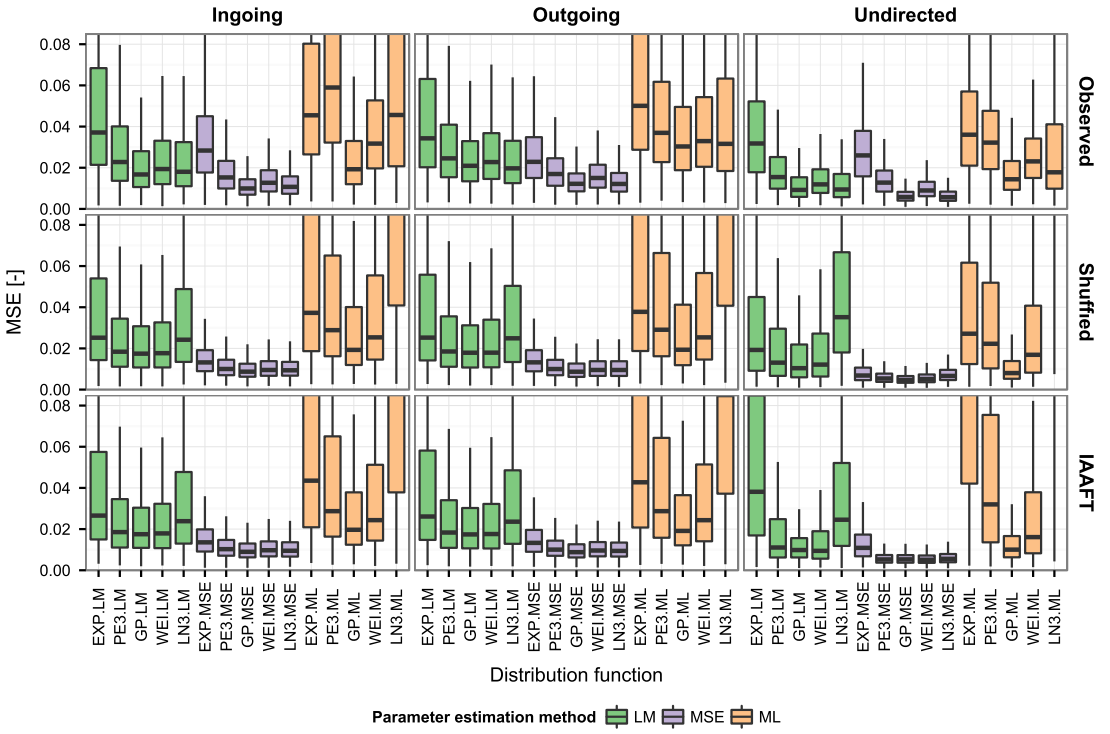

Fig. 5. Box plots of MSE for the five models (EXP, PE3, GP, WEI, and LN3) fitted by the three estimation methods (LM, MSE, and ML). Each panel shows the performance (in terms of MSE) of the five models for the three estimation methods corresponding to each combination of HVG direction (ingoing, outgoing, and undirected) and type of annual data (observed, shuffled, and IAAFT). Comparison should be done among models estimated with the same estimation method. For example, for observed ingoing distributions (top-left panel), GP exhibits the smallest MSE for all the three estimation methods.

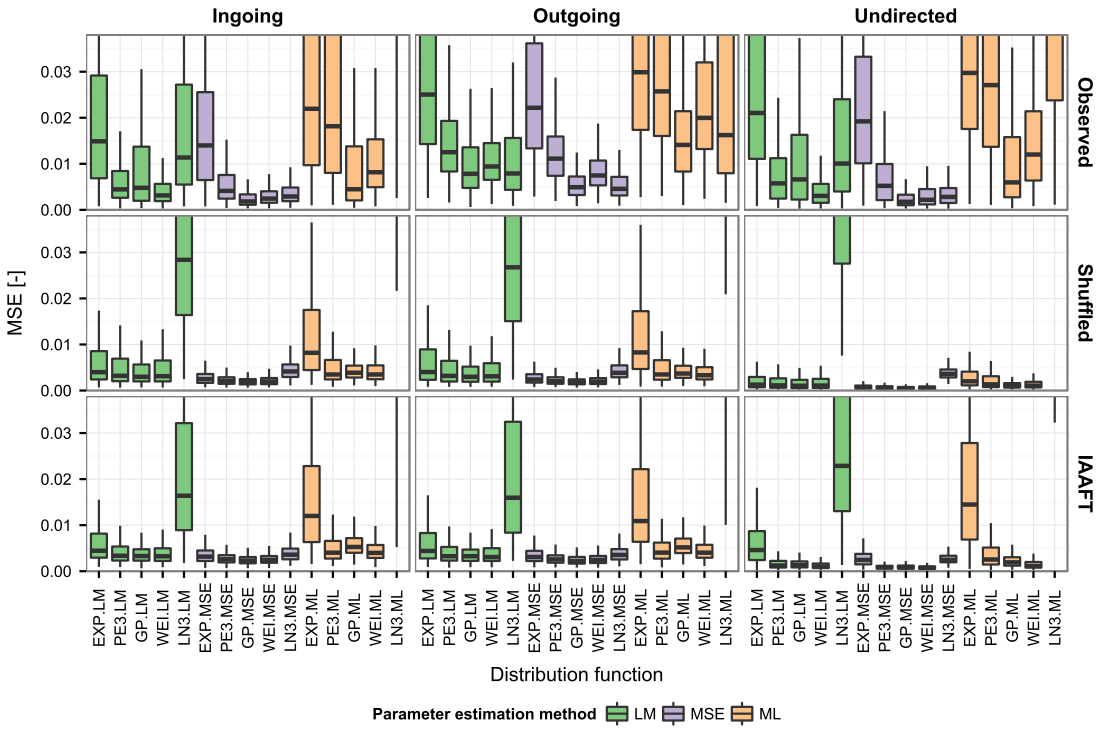

Fig. 6. As for Fig. 5, but for networks defined on the global series; similar interpretation applies.

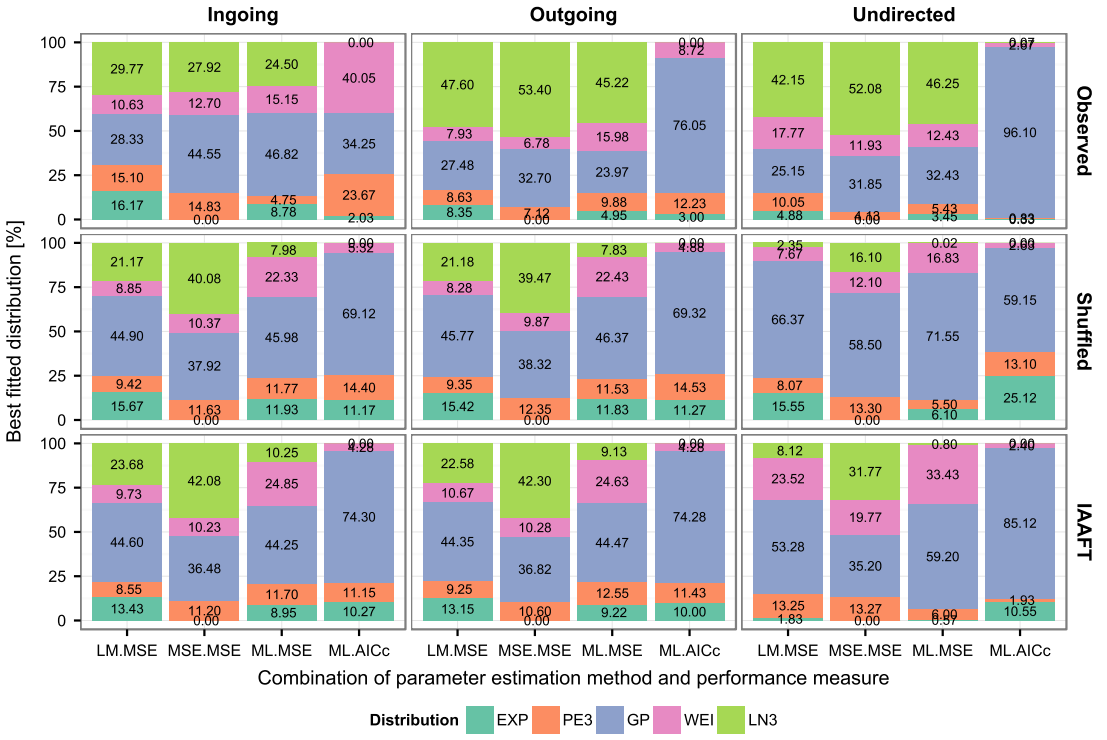

Fig. 7. Comparison of the fitted models in terms of optimal model selection rate. Each bar indicates the percentage of times each model is selected as the best one in terms of minimum MSE or AIC_c. For each panel, the selection rate is reported in terms of MSE for all estimation methods (LM, MSE, and ML), and AIC_c for ML. For example, the first bar in the top-left panel indicates that GP is selected in the 28.33% of times as the best model for observed ingoing degree distributions when parameters are estimated by LM and the goodness of fit is assessed by MSE. For observed data, GP, WEI and LN3 show the highest selection rate depending on the estimation method. GP dominates in terms of AIC_c for outgoing and undirected distributions.

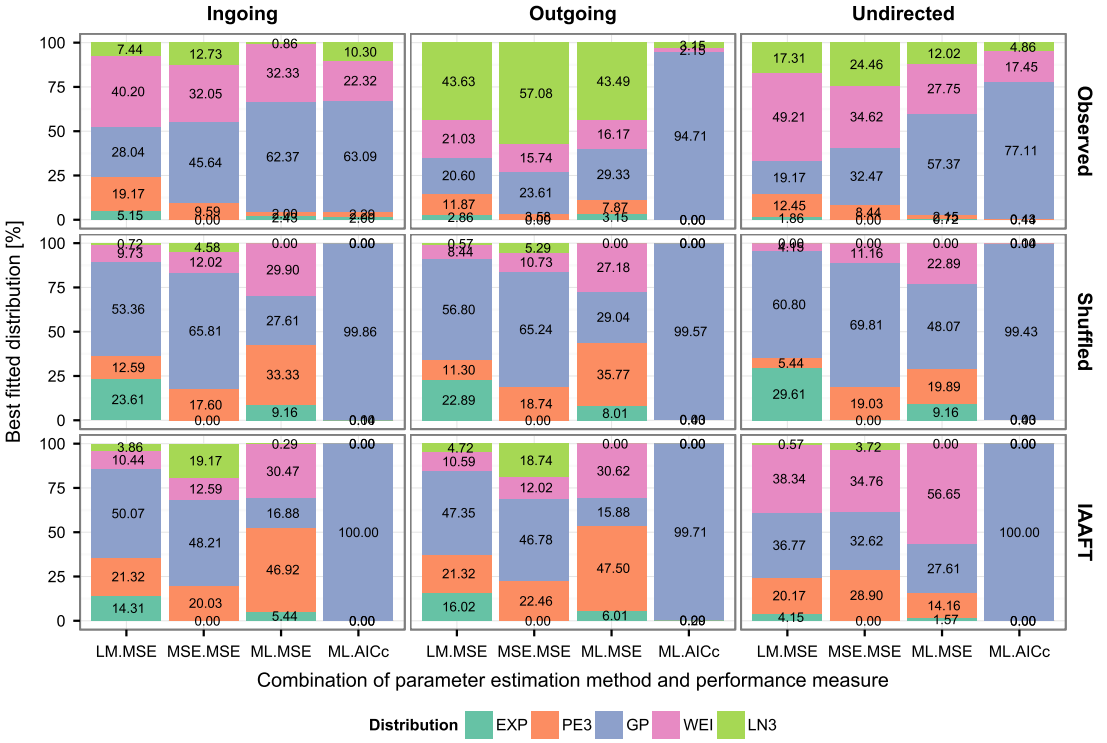

Fig. 8. As for Fig. 7, but for networks defined on the global series; similar interpretation applies. Focusing on observed data, WEI and GP show the highest selection rate for ingoing and undirected distributions, while GP and LN3 are the most frequent optimal models for outgoing distributions.

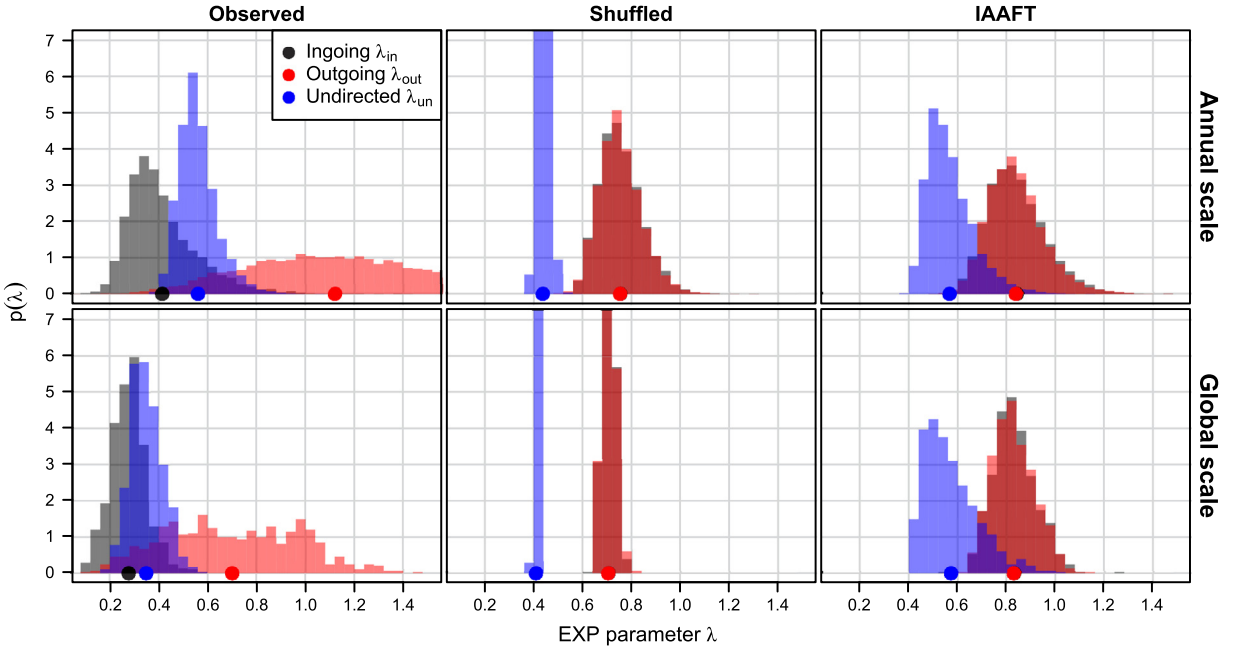

Fig. 9. Empirical PDFs of EXP λ values for the annual (top) and global (bottom) series. Bullet points denote the average values of the samples. Ingoing and outgoing distributions are almost identical for shuffled and IAAFT data (as expected from theoretical results), while they differ for observed data, thus indicating temporal asymmetry and nonlinearity. Shuffled PDFs are centered around the theoretical values $\lambda \approx 0.41$ and $\lambda_{in} = \lambda_{out} \approx 0.69$, while IAAFT signals show greater values corresponding to the expected hyperexponential behavior.

case (see lines intersecting the EXP point in LMRDs shown in Fig. 4). In this respect, the selection of GP, WEI and PE3 as optimal models for shuffled and IAAFT degree distributions is not so surprising.

3.2. Analysis of characteristic parameters

Even though definite conclusion about the true nature of the upper tail of the degree distribution is not possible, the systematic selection of GP as one of the optimal models allows for further analyses. Indeed, the values of the GP shape parameter ξ indicate if the distribution is close to exponential ($\xi \approx 0$) or remarkably subexponential ($\xi > 0$) or hyperexponential ($\xi < 0$). However, when $\xi > 0$ we only conclude that the degree distributions have subexponential behavior without specifying if it is power law or not, because we cannot know if they are actually GP, or e.g. WEI/LN3 with apparent power law behavior. For the sake of comparison and completeness, both EXP λ and GP ξ are studied comparing the PDFs for ingoing λ_{in} (ξ_{in}), outgoing λ_{out} (ξ_{out}), and undirected λ_{un} (ξ_{un}), corresponding to each observed and surrogate (shuffled and IAAFT) series on an annual and global basis. Only MSE estimates are shown as LM and ML have very similar PDFs.

Results for λ are reported in Fig. 9. For observed data, PDFs of λ_{in}, λ_{out}, and λ_{un} are clearly different, being the PDF of λ_{out} shifted on the right side (higher average) and much more dispersed (higher variance). The difference between the PDFs of λ_{in} and λ_{un} reduces at global scale, while λ_{out} values are still the most dispersed. PDFs corresponding to shuffled data agree with the theoretical results, showing empirical averages close to theoretical expected values ($\lambda \approx 0.41$ and $\lambda_{in} = \lambda_{out} \approx 0.69$) and almost identical PDFs for λ_{in} and λ_{out}. This confirms the time symmetry of the shuffled sequences along with the correctness of the implemented algorithm. Compared with shuffled sequences, IAAFT signals are characterized by (directed and undirected) λ values greater than those corresponding to shuffled series [16], and by identical PDFs for λ_{in} and λ_{out}, denoting the linearity of the IAAFT algorithm, which is not able to reproduce the observed irreversibility of flow fluctuations. It should be noted that annual and global PDFs of observed and shuffled data show systematic shifts (bias), and annual PDFs are more dispersed than the global owing to the smaller size of the annual subsets. This further stresses the requirement of larger sample sizes to obtain reliable conclusions.

Assuming GP as a good candidate to explore the behavior of the upper tail of the degree distributions, Fig. 10 shows that in all cases the average values of ξ are close to each other, thus resulting in a broad overlap of the PDFs. Similar to λ, PDFs of ξ_{in} and ξ_{out} for shuffled and IAAFT data are almost indistinguishable (as expected) owing to the signal reversibility. Moreover, the average of ξ_{in} is close to zero confirming the expected convergence to EXP behavior, while the average of ξ_{out} tends to be slightly smaller than zero, indicating the expected hyperexponential decay faster than that of shuffled data. For observed data, the average of ξ_{un} is close to 0.2 with low probability (for global data) to observe negative values. This confirms the subexponential behavior of observed degree distributions even though we cannot draw conclusions about actual or apparent algebraic decay (see discussion in Section 3.1). The pairwise scatter plots and values of Kendall correlation

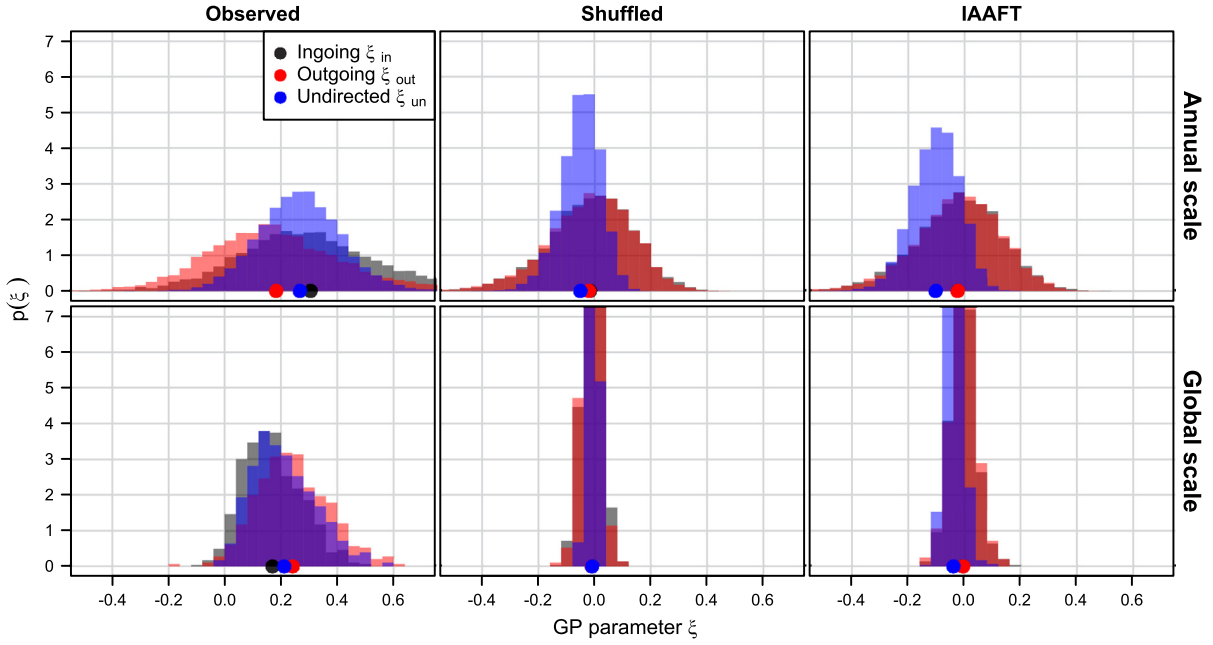

Fig. 10. Empirical PDFs of GP ξ values for the annual (top) and global (bottom) series. Bullet points denote the average values of the samples. As for EXP λ, ingoing and outgoing distributions are almost identical for shuffled and IAAFT data, while they differ for observed data, denoting temporal asymmetry and nonlinearity. Average values are close to zero for shuffled data, indicating GP convergence to EXP; they are slightly negative for IAAFT data, denoting hyperexponential behavior; and ξ averages are close to 0.2 for observed data, thus indicating subexponential behavior.

coefficient in Fig. 11 show that a strong and almost linear relationship does exist between ξ_{un} and ξ_{in} (for observed data), while a weaker and approximately linear relationship characterizes the pairs (ξ_{un}, ξ_{out}) and (ξ_{in}, ξ_{out}). In all cases, ξ values are not related to the logarithm of the drainage basin area, which is a physical quantity that is often related to summary statistics of the stream flow records [13].

These results show that a faithful reproduction of linear properties (autocorrelation/power spectrum) up to second order is not enough to capture a specific feature of stream flow fluctuations related to temporal irreversibility, and thus nonlinearity. The similarity between ingoing and undirected degree distributions shows that the overall degree of each node depends on the number of links with past nodes (observations) more than on links with the future nodes. This can be partly explained by the stream flow dynamics: rising limbs are characterized by faster discharge increases triggered by meteorological impulses that make them "visible" to a number of past observations in the previous recession limb, while the subsequent observations in the slowly decaying recession limb prevent high visibility of many future observations.

We also explored two further aspects: possible spatial patterns of (i) power law exponents, and (ii) correspondence between extreme values and graph's hubs (values characterized by large connectivity). Given the strong relationship between ξ_{un} and ξ_{in}, these parameters show similar spatial patterns with quite coherent clusters of values close to zero in the eastern part of the CONUS, along the Appalachian Mountains and the northern part of the West Coast (Fig. 12(a) and (c)). These clusters tend to disappear for ξ_{out}, whose values are smaller than ξ_{in} and ξ_{un} (see bottom left panel of Fig. 10). Therefore, the behavior of degree distributions, and so, the complex network characterization and nonlinearity of flow fluctuations, are not purely random across the CONUS but are spatially coherent. Since these spatial patterns are likely related to other physical properties, they are worthy of future investigation focusing on local geomorphological characteristics and hydro-meteorological regimes to get deeper insights on flow dynamics. Notice that the cluster of ξ_{un} values close to zero indicate an approximate EXP behavior that is coherent with the findings of Ref. [30]. However, our results show that this behavior can be not general when the analysis is expanded including a larger variety of natural stream flow signals. Moreover, the difference between the spatial patterns of ξ_{in} and ξ_{out} (along with differences in their PDFs) supports the presence of temporally asymmetric dynamics more complex than linear.

For random sequences, extreme high values of flow fluctuations (related to flood events) are expected to be also the most visible nodes with large number of connections/degrees. However, this is not always true for real-world data [23,26] and needs to be checked. We used the following procedure: for each time series, we computed the median $\tilde{y}_{|k}$ of the flow fluctuation values corresponding with each value of degree k resulting from directed and undirected HVGs (i.e., $\tilde{y}_{|k}$ is the median fluctuation conditioned on the discrete values of k); then, the relationship between $\tilde{y}_{|k}$ and k was visually checked for monotonicity and quantified by Kendall correlation coefficient. Kendall correlation values in Fig. 10(d)–(f) show a general positive relationship between flow fluctuation values and k for ingoing and undirected HVGs, thus denoting that the higher values tend to be more connected with past observations. On the other hand, outgoing HVGs yield both positive and negative correlation values with quite a random spatial distribution. Visual inspection (plots not shown) highlighted that the patterns

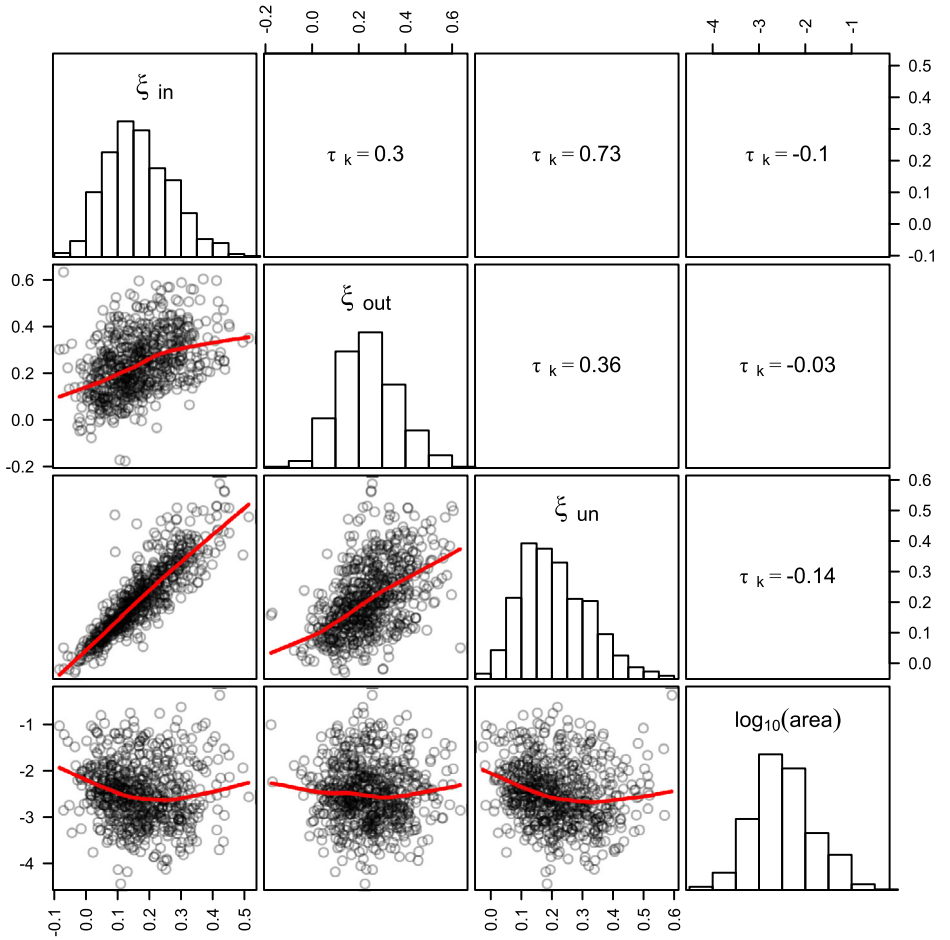

Fig. 11. Scatter plot matrix showing the mutual pairwise relationship between ξ_{in}, ξ_{out}, ξ_{un}, and logarithm of drainage basin area. Lines denote LOESS regression curves. The values of Kendall correlation coefficient are reported in the upper triangular matrix of panels. The diagrams highlight the strong correlation between ξ_{in} and ξ_{un}, and the weak correlation between ξ values and drainage basin area.

of $\tilde{y}_{|k}$ versus k can be non monotonic, thus resulting in mixed results. These differences further stress the nonlinear effect of the different physical dynamics acting in the rising and recession phases of the flow process.

4. Conclusions

In this study, directed and undirected HVG algorithm developed in complex network theory has been applied for the first time on a large high quality data set of stream flow fluctuations with length up to 114 years recorded across the CONUS area. The analysis of ingoing, outgoing, and undirected degree distributions related to the network representation of the time series allowed us to highlight the nonlinear behavior of natural flow fluctuations free from anthropogenic influence. Nonlinearity is characterized in terms of irreversibility and interpreted as a consequence of the different physical processes triggering the rising and recession limbs of the hydrograph. A detailed analysis of degree distributions showed a systematic subexponential behavior of various strength, going from approximately exponential to apparent power law with well defined spatial patterns across the study area. However, the sampling uncertainty does not allow definite conclusions about the true nature of the upper tails, i.e. apparent or true power law behavior. These results are corroborated by an extensive comparison involving suitable surrogate data preserving almost exactly up to the second order linear properties. Our findings show that flow dynamics are more complex than simple stochastic linear dynamics, and irreversibility is a key feature to get insights on the nonlinearity of the flow process. This study extends recent analyses concerning a large set of Brazilian stream flow records [30], and shows a rather different behavior for North-American rivers, for which nonlinearity seems to be the dominant characteristic, concealing the underlying short and long range linear dynamics. Our findings contribute to pave the way for further investigations based on tools developed in network theory, as well as the development of suitable models to account for irreversibility. Combining "temporal" network analysis and "spatial" network analysis recently introduced in hydrological sciences [54–58] is also another topic deserving further research for a better understanding of stream flows and other geophysical processes.

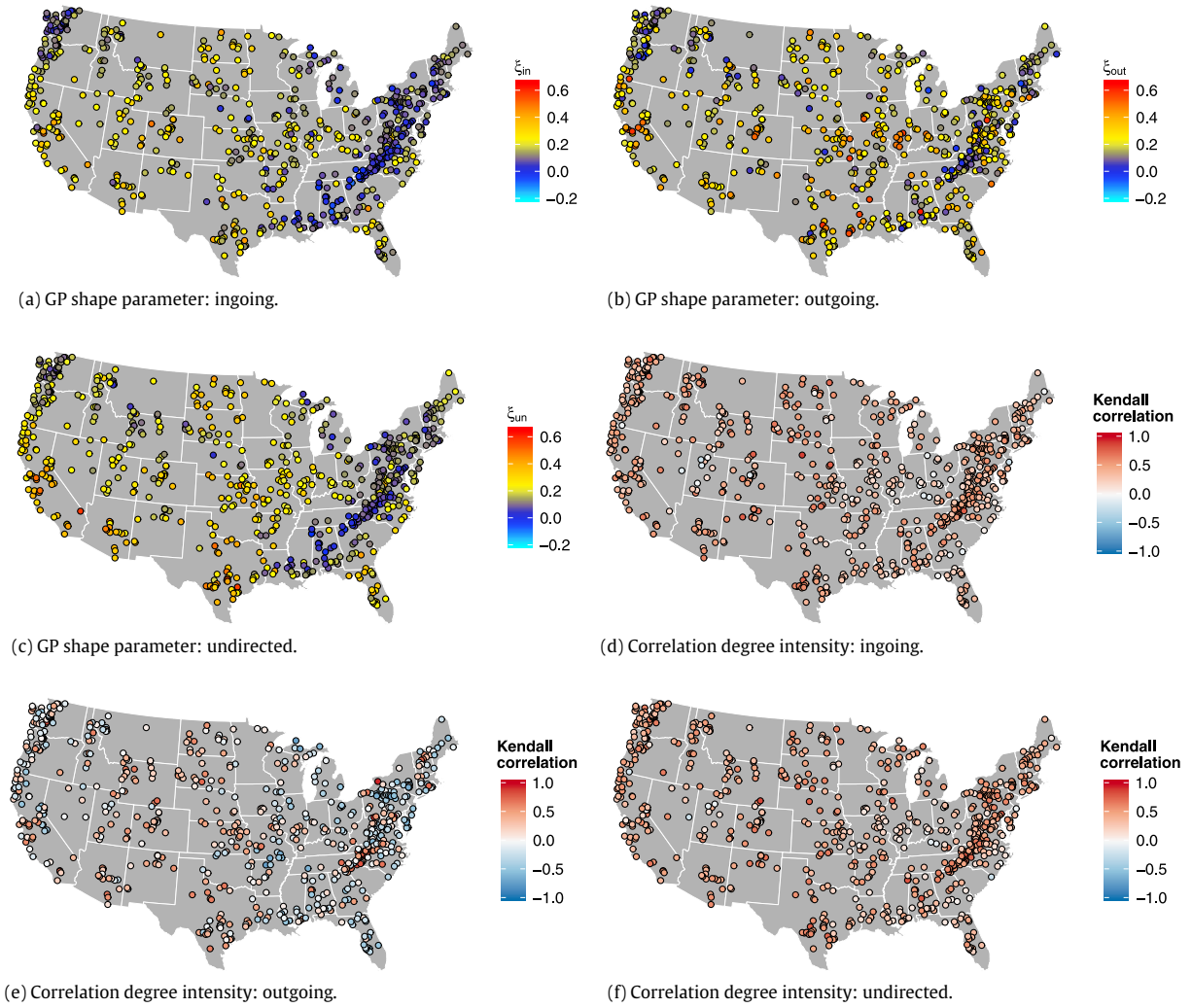

(a) GP shape parameter: ingoing.

(b) GP shape parameter: outgoing.

(c) GP shape parameter: undirected.

(d) Correlation degree intensity: ingoing.

(e) Correlation degree intensity: outgoing.

(f) Correlation degree intensity: undirected.

Fig. 12. Spatial patterns of ξ_{in} (a), ξ_{out} (b), and ξ_{un} (c), and Kendall correlation coefficient of the pairs $(k, \tilde{y}_{|k})$ for ingoing, outgoing, and undirected HVGs (d–f). Panels (a) and (b) show two clusters of degree distributions with approximately exponential behavior ($\xi_{in}, \xi_{un} \approx 0$) along the Appalachian Mountains and the northern part of the West Coast. The clusters tend to disappear for ξ_{out}, denoting a widespread subexponential behavior. Panels (d–f) show general positive correlation between the pairs $(k, \tilde{y}_{|k})$ for ingoing and undirected HVGs, and quite a random spatial variability around zero for outgoing HVGs.

Acknowledgments

This work was supported by the Engineering and Physical Sciences Research Council (EPSRC) grant EP/K013513/1 "Flood MEMORY: Multi-Event Modelling Of Risk & recoverY", and Willis Research Network. The authors wish to thank Dr. Haroldo V. Ribeiro (Universidade Estadual de Maringá, Brazil) and two anonymous reviewers for their remarks that helped improve the quality of the original manuscript. The analyses were performed in R [59] by using the contributed package `lmom` [60].

Appendix

The five distributions used in this study are parameterized as follows [49, pp. 192–201].

Exponential distribution (EXP):

$$F(x; \mu, \lambda) = 1 - \exp\left(-\frac{x-\mu}{\lambda}\right), \tag{A.1}$$

where $x \geq \mu$, $\mu \in \mathbb{R}$ is the lower endpoint of the distribution, and λ is a scale parameter.

Pearson type III (PE3):

$$F(x; \mu, \lambda, \xi) = \Gamma\left(\xi, \frac{x-\mu}{\lambda}\right) / \Gamma(\xi), \tag{A.2}$$

where $x \geq \mu$, $\Gamma(\xi, x) = \int_0^x t^{\xi-1}\mathrm{e}^{-t}\mathrm{d}t$, $\Gamma(\xi) = \int_0^\infty t^{\xi-1}\mathrm{e}^{-t}\mathrm{d}t$, $\mu \in \mathbb{R}$ is the lower endpoint of the distribution, $\lambda > 0$ is a scale parameter, and $\sqrt{\xi} > 0$ is a shape parameter.

Generalized Pareto (GP):

$$F(x; \mu, \lambda, \xi) = \begin{cases} 1 - \left(1 + \xi \dfrac{x-\mu}{\lambda}\right)^{-1/\xi} & \text{if } \xi \neq 0 \\ 1 - \exp\left(-\dfrac{x-\mu}{\lambda}\right) & \text{if } \xi = 0, \end{cases} \tag{A.3}$$

where $x \in [\mu, \mu + \lambda/\xi]$ if $\xi < 0$, $x \geq \mu$ if $\xi \geq 0$, $\mu \in \mathbb{R}$ is a location parameter, $\lambda > 0$ is a scale parameter, and $\xi \in \mathbb{R}$ is a shape parameter. For $\xi = 0$, GP converges to EXP; for $\xi = 1$, Eq. (A.3) yields a uniform distribution on the interval $x \in [\mu, \mu + \lambda]$.

Weibull (WEI):

$$F(x; \mu, \lambda, \xi) = 1 - \exp\left(-\left(\frac{x-\mu}{\lambda}\right)^{\xi}\right), \tag{A.4}$$

where $x \geq \mu$, $\mu \in \mathbb{R}$ is the lower endpoint of the distribution, $\lambda > 0$ is a scale parameter, and $\xi > 0$ is a shape parameter.

Lognormal (LN3):

$$F(x; \mu, \lambda, \xi) = \Phi\left(\frac{\log(x-\mu) - \lambda}{\xi}\right) = \Phi\left(\log\left(\frac{(x-\mu)^{1/\xi}}{\exp(\lambda/\xi)}\right)\right), \tag{A.5}$$

where $x > \mu$, $\mu \in \mathbb{R}$ is the lower endpoint of the distribution, $\lambda > 0$ is a scale parameter, while $\xi > 0$ controls the shape of the distribution as is better highlighted by the third term of Eq. (A.5).

References

[1] L. Lacasa, A. Nunez, É Roldán, J.M. Parrondo, B. Luque, Time series irreversibility: a visibility graph approach, Eur. Phys. J. B 85 (2012) 1–11.
[2] R. Kawai, J.M.R. Parrondo, C. Van den Broeck, Dissipation: The phase-space perspective, Phys. Rev. Lett. 98 (2007) 080602.
[3] J.M.R. Parrondo, C. Van den Broeck, R. Kawai, Entropy production and the arrow of time, New J. Phys. 11 (2009) 073008.
[4] F. Serinaldi, C.G. Kilsby, Understanding persistence to avoid underestimation of collective flood risk (submitted for publication) 2015.
[5] T. Schreiber, A. Schmitz, Surrogate time series, Physica D 142 (2000) 346–382.
[6] H.E. Hurst, Long-term storage capacity of reservoirs, Trans. Amer. Soc. Civ. Eng. 116 (1951) 770–808.
[7] K.W. Hipel, A.I. McLeod, Time Series Modelling of Water Resources and Environmental Systems, in: Developments in Water Science, Elsevier Science, 1994.
[8] A. Montanari, R. Rosso, M.S. Taqqu, Fractionally differenced ARIMA models applied to hydrologic time series: Identification, estimation, and simulation, Water Resour. Res. 33 (1997) 1035–1044.
[9] A. Montanari, R. Rosso, M.S. Taqqu, A seasonal fractional ARIMA model applied to the Nile River monthly flows at Aswan, Water Resour. Res. 36 (2000) 1249–1259.
[10] D. Koutsoyiannis, HESS Opinions A random walk on water, Hydrol. Earth Syst. Sci. 14 (2010) 585–601.
[11] D. Koutsoyiannis, Hurst–Kolmogorov dynamics and uncertainty, J. Am. Water Resour. Assoc. 47 (2011) 481–495.
[12] P. Dimitriadis, D. Koutsoyiannis, Climacogram versus autocovariance and power spectrum in stochastic modelling for Markovian and Hurst–Kolmogorov processes, Stoch. Environ. Res. Risk Assess. (2015) 1–21.
[13] F. Serinaldi, L. Zunino, O. Rosso, Complexity-entropy analysis of daily stream flow time series in the continental United States, Stoch. Environ. Res. Risk Assess. 28 (2014) 1685–1708.
[14] J.O. Pierini, J.C. Restrepo, M. Lovallo, L. Telesca, Discriminating between different streamflow regimes by using the Fisher–Shannon method: An application to the Colombia rivers, Acta Geophys. (2014) 1–14.
[15] A. Shaban, L. Telesca, T. Darwich, N. Amacha, Analysis of long–term fluctuations in stream flow time series: An application to Litani River, Lebanon, Acta Geophys. 62 (2014) 164–179.
[16] L. Lacasa, R. Toral, Description of stochastic and chaotic series using visibility graphs, Phys. Rev. E 82 (2010) 036120.
[17] A.S.L.O. Campanharo, M.I. Sirer, R.D. Malmgren, F.M. Ramos, L.A.N. Amaral, Duality between time series and networks, PLoS One 6 (2011) e23378.
[18] A. Murks, M. Perc, Evolutionary games on visibility graphs, Adv. Complex Syst. 14 (2011) 307–315.
[19] A.S. Campanharo, F.M. Ramos, Hurst exponent estimation of self-affine time series using quantile graphs, Physica A 444 (2016) 43–48.
[20] L. Lacasa, B. Luque, F. Ballesteros, J. Luque, J.C. Nuno, From time series to complex networks: The visibility graph, Proc. Natl. Acad. Sci. 105 (2008) 4972–4975.
[21] L. Lacasa, B. Luque, J. Luque, J.C. Nuno, The visibility graph: A new method for estimating the Hurst exponent of fractional Brownian motion, Europhys. Lett. 86 (2009) 30001.
[22] J.B. Elsner, T.H. Jagger, E.A. Fogarty, Visibility network of United States hurricanes, Geophys. Res. Lett. 36 (2009) L16702.
[23] L. Telesca, M. Lovallo, Analysis of seismic sequences by using the method of visibility graph, Europhys. Lett. 97 (2012) 50002.
[24] L. Telesca, M. Lovallo, L. Toth, Visibility graph analysis of 2002–2011 Pannonian seismicity, Physica A 416 (2014) 219–224.
[25] L. Telesca, M. Lovallo, J.O. Pierini, Visibility graph approach to the analysis of ocean tidal records, Chaos Solitons Fractals 45 (2012) 1086–1091.
[26] J.O. Pierini, M. Lovallo, L. Telesca, Visibility graph analysis of wind speed records measured in central Argentina, Physica A 391 (2012) 5041–5048.
[27] Y. Zou, R.V. Donner, N. Marwan, M. Small, J. Kurths, Long-term changes in the North–South asymmetry of solar activity: a nonlinear dynamics characterization using visibility graphs, Nonlinear Processes Geophys. 21 (2014) 1113–1126.
[28] B. Luque, L. Lacasa, F. Ballesteros, J. Luque, Horizontal visibility graphs: Exact results for random time series, Phys. Rev. E 80 (2009) 046103.
[29] J.F. Donges, R.V. Donner, J. Kurths, Testing time series irreversibility using complex network methods, Europhys. Lett. 102 (2013) 10004.
[30] A.C. Braga, L.G.A. Alves, L.S. Costa, A.A. Ribeiro, M.M.A. de Jesus, A.A. Tateishi, H.V. Ribeiro, Characterization of river flow fluctuations via horizontal visibility graphs, Physica A 444 (2016) 1003–1011.
[31] H. Lins, Hydro-Climatic Data Network 2009 (HCDN-2009), US Geological Survey Fact Sheet 2012–3047, 2012. URL: http://pubs.usgs.gov/fs/2012/3047/.
[32] W.S. Cleveland, S.J. Devlin, Locally-weighted regression: An approach to regression analysis by local fitting, J. Amer. Statist. Assoc. 83 (1988) 596–610.
[33] R.B. Cleveland, W.S. Cleveland, J.E. McRae, I. Terpenning, STL: A seasonal-trend decomposition procedure based on loess, J. Off. Stat. 6 (1990) 3–73.

[34] J.W. Kantelhardt, E. Koscielny-Bunde, D. Rybski, P. Braun, A. Bunde, S. Havlin, Long-term persistence and multifractality of precipitation and river runoff records, J. Geophys. Res.: Atmos. 111 (2006) D01106.
[35] T. Schreiber, A. Schmitz, Improved surrogate data for nonlinearity tests, Phys. Rev. Lett. 77 (1996) 635–638.
[36] D. Kugiumtzis, Test your surrogate data before you test for nonlinearity, Phys. Rev. E 60 (1999) 2808–2816.
[37] V. Venema, F. Ament, C. Simmer, A stochastic iterative amplitude adjusted Fourier transform algorithm with improved accuracy, Nonlinear Processes Geophys. 13 (2006) 321–328.
[38] V. Venema, S. Bachner, H.W. Rust, C. Simmer, Statistical characteristics of surrogate data based on geophysical measurements, Nonlinear Processes Geophys. 13 (2006) 449–466.
[39] C. Franzke, A novel method to test for significant trends in extreme values in serially dependent time series, Geophys. Res. Lett. 40 (2013) 1391–1395.
[40] P. Embrechts, C. Klüppelberg, T. Mikosch, Modelling Extremal Events for Insurance and Finance, Springer, Berlin, 1997.
[41] S. El Adlouni, B. Bobée, T.B.M.J. Ouarda, On the tails of extreme event distributions in hydrology, J. Hydrol. 355 (2008) 16–33.
[42] S.M. Papalexiou, D. Koutsoyiannis, C. Makropoulos, How extreme is extreme? An assessment of daily rainfall distribution tails, Hydrol. Earth Syst. Sci. 17 (2013) 851–862.
[43] N.J. Cook, R. Harris, Exact and general FT1 penultimate distributions of extreme wind speeds drawn from tail-equivalent Weibull parents, Struct. Saf. 26 (2004) 391–420.
[44] R.-D. Reiss, M. Thomas, Statistical Analysis of Extreme Values: With Applications to Insurance, Finance, Hydrology and Other Fields, third ed., Birkhäuser, Basel, 2007.
[45] E.M. Furrer, R.W. Katz, Improving the simulation of extreme precipitation events by stochastic weather generators, Water Resour. Res. 44 (2008) W12439.
[46] M. Mitzenmacher, A brief history of generative models for power law and lognormal distributions, Internet Math. 1 (2004) 226–251.
[47] P. Cirillo, Are your data really Pareto distributed? Physica A 392 (2013) 5947–5962.
[48] J.R.M. Hosking, L-moments: analysis and estimation of distributions using linear combinations of order statistics, J. R. Stat. Soc. Ser. B 52 (1990) 105–124.
[49] J.R.M. Hosking, J.R. Wallis, Regional Frequency Analysis: An Approach Based on L-Moments, Cambridge University Press, New York, 1997.
[50] F. Laio, Cramer–von Mises and Anderson–Darling goodness of fit tests for extreme value distributions with unknown parameters, Water Resour. Res. 40 (2004) W09308.
[51] K.P. Burnham, D.R. Anderson, Model Selection and Multimodel Inference: A Practical Information-Theoretic Approach, second ed., Springer, New York, 2002.
[52] H. Akaike, A new look at the statistical model identification, IEEE Trans. Automat. Control 19 (1974) 716–723.
[53] M. Perc, The Matthew effect in empirical data, J. R. Soc. Interface 11 (2014) 1–15.
[54] S. Scarsoglio, F. Laio, L. Ridolfi, Climate dynamics: a network-based approach for the analysis of global precipitation, PLoS One 8 (2013) e71129.
[55] B. Sivakumar, F.M. Woldemeskel, Complex networks for streamflow dynamics, Hydrol. Earth Syst. Sci. Discuss. 11 (2014) 7255–7289.
[56] B. Sivakumar, F.M. Woldemeskel, A network-based analysis of spatial rainfall connections, Environ. Modell. Softw. 69 (2015) 55–62.
[57] B. Sivakumar, Networks: a generic theory for hydrology? Stoch. Environ. Res. Risk Assess. 29 (2015) 761–771.
[58] S.K. Jha, H. Zhao, F.M. Woldemeskel, B. Sivakumar, Network theory and spatial rainfall connections: An interpretation, J. Hydrol. 527 (2015) 13–19.
[59] R Development Core Team, R: A Language and Environment for Statistical Computing, R Foundation for Statistical Computing, Vienna, Austria, ISBN: 3-900051-07-0, 2015, URL: http://www.R-project.org/.
[60] J.R.M. Hosking, L-moments, 2014. R package, version. 2.4 URL:http://CRAN.R-project.org/package=lmom.